BOND BEHAVIOR OF STEEL FIBER REINFORCED MORTAR (SFRM) APPLIED ONTO MASONRY SUBSTRATE

Paolo Zampieri*, Nicolò Simoncello, Jaime Gonzalez, Carlo Pellegrino

Department of Civil, Environmental and Architectural Engineering, University of Padova.

*paolo.zampieri@dicea.unipd.it, corresponding Author.

ABSTRACT

Masonry was the most used material during the last centuries to build constructions. Most of the existing masonry structures (buildings, bridges etc.) were built without considering some important structural considerations that are important nowadays. Moreover, due to factors such as the increasing of service loads, materials aging, structural damage, etc., existing masonry structures require strengthening interventions. The definition of optimal strengthening strategies using traditional and innovative materials is still an important issue of the scientific research. In fact, during the last decade, many researchers focused their attention studying innovative composites materials, such as fiber-reinforced polymers (FRP) and fiber-reinforced cementitious matrix (FRCM) composites, for the strengthening of existing masonry structures. This research has focused on aspects such as the bond behavior between the substrate and the composite materials, the structural behavior of the strengthened masonry and concrete structures, and the compatibility and reversibility of these materials when bonded to existing substrates. In this study, the bond behavior of a composite material known as steel fiber-reinforced mortar (SFRM), recently used as for the strengthening of existing structures, applied onto masonry structures is analyzed experimentally and numerically. First, the material is characterized experimentally with the aim of getting insight on its behavior and applicability when applied as an innovative technique for the strengthening of masonry and to obtain mechanical parameters required for the numerical models. Mechanical properties of the SFRM

studied included flexural and compressive strength, tensile strength, and residual flexural strength. The SFRM bond behavior on masonry substrates was evaluated by means of double shear lap tests. In addition, the experimental tensile and bond behavior of the SFRM is studied numerically through finite element models validated using the results obtained during the experimental tests. Results show that if an adequate bonded length is provided, the SFRM can fully develop its tensile strength as detachment from the substrate is not observed.

Keywords: steel fiber reinforced mortar (SFRM); masonry; strengthening; mechanical characterization; bond behavior, tensile test, numerical modelling.

1. INTRODUCTION

The interest to preserve old masonry structures has caught the attention of the scientific community and civil engineering industry. This interest has led to the development of many techniques used to improve the structural safety level of masonry structures and reduce their structural vulnerability. One of the first techniques employed consisted in the use of steel applied to masonry structural elements with the aim of increasing their compression, flexural, and shear strength [1]. However, with the gain in knowledge regarding the behavior of strengthened masonry structures, such traditional techniques have been replaced by the use of externally bonded composite materials, such as fiber reinforced polymers (FRP) [2-5], and fiber reinforced cementitious matrix (FRCM) composites [6-10].

These composite materials can also improve the confinement, flexural and shear strengths of the masonry structural elements with a low weight increment. In addition, their application to straight and curved surfaces is easily performed due to its mode of application [11]. However, some disadvantages deserve to be considered. For FRP composites, the vapor permeability of the masonry structures can be compromised due to the epoxy resin used for the adhesion of the fibers to masonry substrates. Other disadvantages are related to the inability to apply the FRP at low temperatures or on wet surfaces [12]. Instead, FRCM composites are able to overcome some of these disadvantages. In fact, during the last decade, the epoxy resin has started to be substituted with the cementitious matrix that is more compatible with masonry materials [10, 13]. However, a recent study has pointed out that the application of FRCM has a lower increase in the load-carrying capacity when compared to FRP, but it promotes a higher increase in the ductility [14, 15].

Recently, the interest in the use of fiber reinforced concrete (FRC) or mortar (FRM) composites, comprised of an ultra-high performance concrete or mortar and short fibers, as strengthening material is a growing research field but, due to its novelty, the available scientific literature on the topic is quite limited. In fact, the use of these materials has been generally studied as a construction material for the design of new structural elements [16,17] and the experimental and numerical research has focused on the evaluation of its mechanical properties (uniaxial tensile strength and tensile fracture properties [18], etc.), the behavior of new high performance reinforced concrete elements [19], the ultimate shear behavior of hybrid RC beam and steel columns [20], or its use on building applications such as non-structural elements, for instance. In these cases, the presence of the fibers improves the mechanical properties of the building material and allows decreasing the area of steel reinforcement.

As strengthening material, FRC or FRM has been studied as an externally bonded strengthening system applied onto concrete bridge piers [21], masonry walls [22, 23], or at the intrados of masonry arches [24], with promising results. Among the advantages of FRC or FRM, it can be noticed that the use of high performance cementitious matrix guarantees an adequate vapor permeability with considerable abrasion resistance and high durability [25]. Furthermore, its high compressive strength can provide an increase in the compressive resistance of the structural element, which is not achieved when FRP or FRCM composites are used. In addition, the flowability and self-compacting properties of the material allow filling simple traditional formwork which facilitates its application on the elements to be strengthened.

As for the case of another available externally bonded strengthened systems, such as FRCM and FRP composite materials, in which those issues have been more extensively discussed and studied, knowledge on the bond behavior of these materials when applied onto existing substrates issues is crucial for the understanding of the overall behavior of FRC/FRM strengthened structures. Available literature in the topic has focused mainly on the study of such materials applied onto normal compressive strength substrates for either repair or strengthening applications. As repair material, the bond behavior has been studied by means of slant shear, splitting tensile, and direct tensile tests, which do not replicate exactly the conditions expected when the material is externally bonded as a strengthening solution [26, 27]. As for strengthening material, Zhang et al 2020 [28] have recently investigated the shear bond strength of FRC applied onto concrete by means of double-sided direct shear tests. The test results showed that the interface between the FRC and the substrate exhibited an excellent bond behavior, which verifies the feasibility of the use of these materials for the strengthening of existing structures. In their research, the most common failure mode of the specimens was associated with partial interface failure with partial or complete failure in shear of the substrate. However, on the authors' knowledge, there is no experimental evidence on the study of the bond behavior of these materials when applied to masonry substrates.

Based on this requirement, this paper is aimed to provide an exhaustive experimental and numerical analysis of the bond behavior of a type of FRM comprised of a high performance mortar and short steel fibers, known as steel fiber-reinforced mortar (SFRM), when applied onto masonry substrates. The bond behavior was investigated through double shear lap tests (conducted with two different bonded lengths) and observations on peak load and failure mode are highlighted. The material is also mechanically characterized by means of flexural, compressive, direct tensile, and residual flexural tests with the aim of obtaining the parameters required for the numerical modelling presented in the paper.

2. MASONRY EXPERIMENTAL CHARACTERIZATION

2.1. Masonry mortar characterization

An M5 class mortar (according to UNI EN 998–2_2016 [29]) was used for the realization of the masonry specimens used for the shear lap tests and experimentally characterized. This mortar consists in a Portland cementitious matrix with hydrated lime. The water required for the mortar hydration was of around 18% of the mortar weight while the maximum aggregate size is lower than 3 mm. The mixing procedure was carried out by means of a mixer machine for three minutes. According to the manufacturer, the workability time of the mortar matrix is of around two hours. Before the application of mortars, the clay bricks were wetted. After casting of the joints, the samples were left to dry under environmental conditions.

For the mortar characterization, six mortar prismatic elements with 40 x 40 mm of cross-section and 160 mm length were built in order to evaluate the flexural (f_{fm}) and compressive (f_m) strength, and the elastic modulus (E_m) of the mortar according to standards UNI EN 1015-11 [30] and EN 13412 [31], respectively. In Table 1, the corresponding mean values and coefficient of variations (CoV) of these parameters are shown.

Table 1. Mortar mechanical properties.

Material	Density	Compressive strength (f_m)		Flexural strength (f_{fm})		Elastic Modulus (E_m)	
	[kg/m^3]	[MPa]	CoV [%]	[MPa]	CoV [%]	[MPa]	CoV [%]
Masonry joint mortar (28 days)	1807	7.22	9.88	2.22	4.61	3706	16.33
SFRM matrix mortar (28 days)	2402	91.02	1.59	15.43	11.98	24040	22.01

2.1. Clay bricks characterization

Solid clay bricks (Euroformat type) fired in a furnace near Venice (Italy) were used in the experimental campaign and were tested to evaluate their compressive and flexural strengths.

Three bricks (named A, B, and C) with length (*l*), width (*b*) and height (*d*) shown in Table 2 were tested following the requirements reported in BS EN 771-1:2011 [32]. Before testing, the clay bricks were subjected to geometrical preparation in order to eliminate any geometrical imperfection caused by the fired process. With this aim, the specimens were cut to create planar faces with a circular saw. After cutting, the specimens were leveled again with an abrasion process aiming to obtain an adequate dimension accuracy.

The elastic modulus was evaluated considering three specimens with dimensions 58 x 58 x 233 mm^3 (see Fig. 1). The load was applied in three load cycles considering maximum amplitudes equal to 7.82, 11.24, and 14.67 N/mm^2. The elastic modulus was then defined during the last cycle using four DD1 strain transducers applied in the middle of the four faces of the specimens. The values of weight, compressive and flexural strengths, and elastic modulus for the specimens tested and the corresponding mean values and coefficient of variations (CoV) are reported in Table 2.

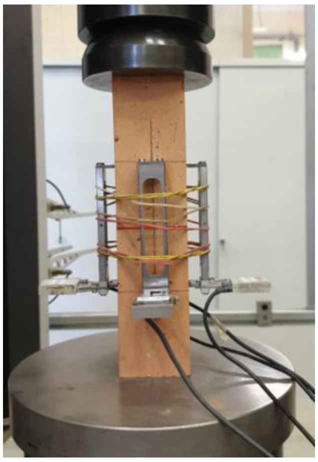

Fig. 1. Elastic modulus for clay bricks.

Table 2. Brick mechanical properties.

Test	Brick weight	l	d	h	Compressive strength		Flexural strength		Elastic Modulus	
	[kg]	[mm]	[mm]	[mm]	[MPa]	CoV [%]	[MPa]	CoV [%]	[MPa]	CoV [%]
A	2.71	245	111	57	46.2		3.69		8850	
B	2.68	243	110	58	40.7		2.76		8750	
C	2.72	245	111	58	45.1		5.73		8500	
Mean value					44.0	6.61	4.06	37.4	8700	2.07

2.2. Masonry characterization

Three masonry prisms (named MPT), with cross-section dimensions l=245 mm and d=110 mm and a total height of 370 mm, were built to evaluate the masonry compressive strength ($f_{c,p}$) and elastic modulus (E_p). The prisms included five rows of clay bricks and six mortar joints with an average thickness of 12 mm, as shown in Fig. 2a.

For the masonry prisms, the tests were conducted (according BS EN 1052-1-1999 [33] using a uniaxial machine with a cell with a maximum capacity of around 60 tons. The stress was obtained dividing the applied load by the average cross-section area of the specimen. The strains were computed as the average value obtained using four linear transducers (LVDTs) placed onto the masonry and fixed by dowels (Figs. 2a and 2b). The gage length of the LVDTs was around 1/3 of the specimens' height (Figs. 2a and 2b).

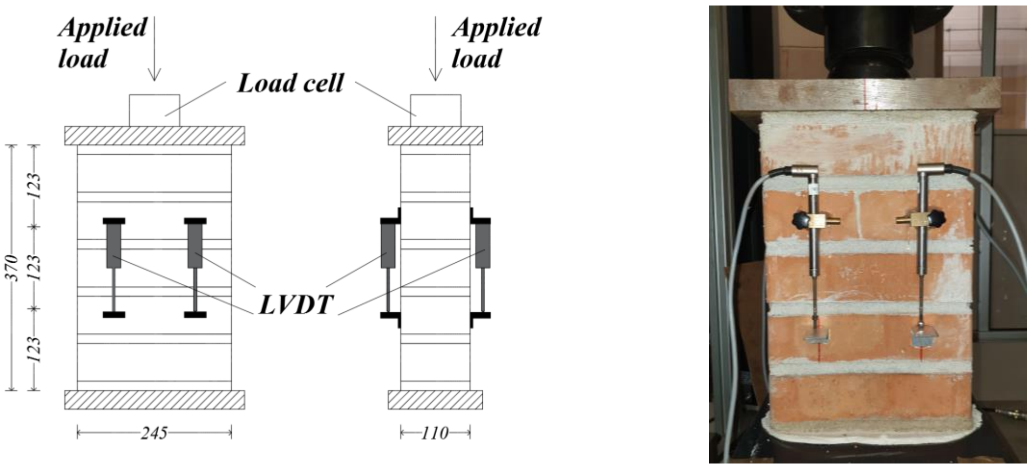

a) b)

Fig. 2. Masonry uniaxial compression: a) test setup, b) specimen being tested.

The masonry prism compressive strength ($f_{c,p}$) was evaluated using following equation:

$$f_{c,p} = P_{max}/(l \cdot d) \qquad (1)$$

where P_{max} is the maximum applied load recorded during the tests. The elastic modulus (E_p) was computed as:

$$E_p = \frac{P_{max}/3}{[l \cdot d \cdot \varepsilon(\frac{F_{max}}{3})]} \qquad (2)$$

Where $\varepsilon(P_{max}/3)$ is the strain measured at $P_{max}/3$. Values of $f_{c,p}$, ultimate compressive strain ($\varepsilon_{u,p}$), and E_p for the three masonry prisms and the corresponding mean value and coefficient of variation (CoV) are presented in Table 3. In Fig. 3, the normal stress-strain curves obtained from the compressive tests are shown.

Table 3. Masonry prism mechanical properties

	Compressive Strength ($f_{c,p}$)		Ultimate compressive strain ($\varepsilon_{u,p}$)		Elastic Modulus (E_p)	
	[MPa]	CoV [%]	[%]	CoV [%]	[MPa]	CoV [%]
MPT_001	18.9		0.377		8800	
MPT_002	20.0		0.403		6100	
MPT_003	19.7		0.363		7500	
Mean value	19.5	2.91	0.381	5.33	7500	18.08

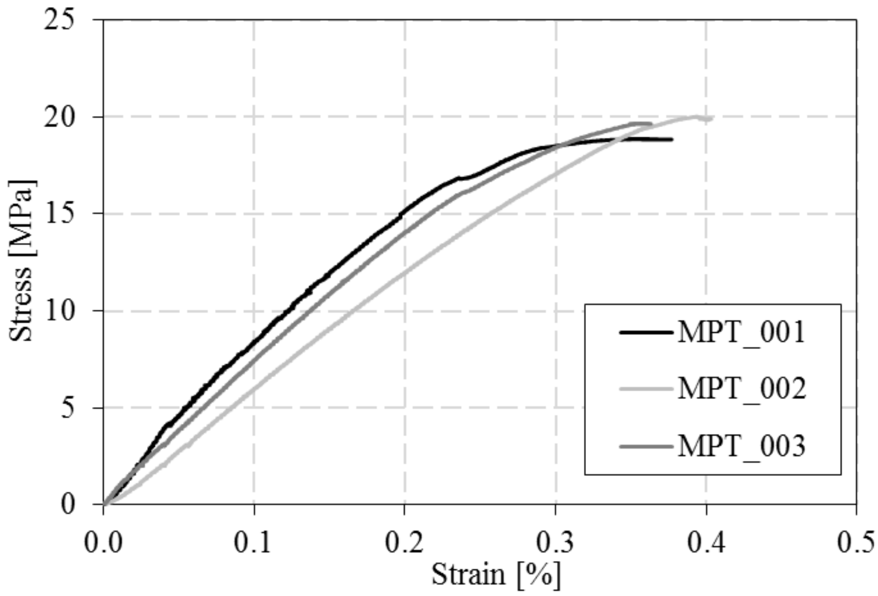

Fig. 3. Normal compressive Stress - Strain curves of masonry prisms.

As shown in Fig. 4, cracks running parallel to the vertical axis of the specimens and concentrated mainly at the center of the elements were observed at the end of the test.

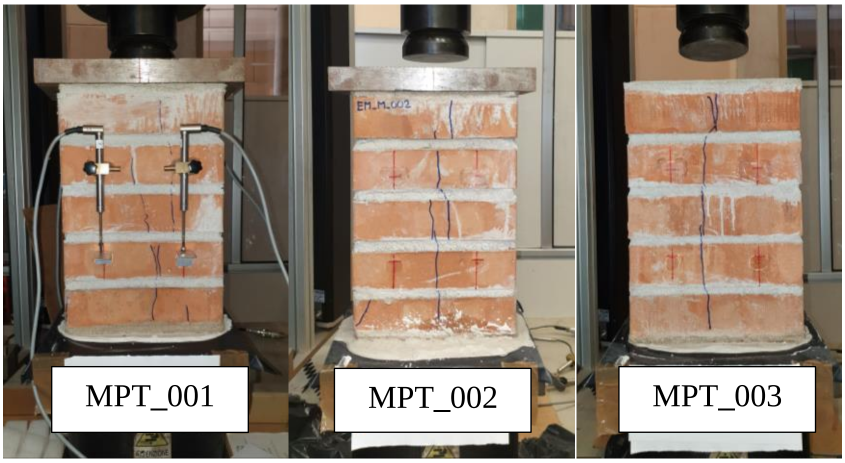

Fig. 4. Failure modes of the masonry prisms.

The characteristic masonry compressive strength ($f_{ck,p}$) derived from compressive experimental tests is compared with that found using the analytical formulation (named $f_{ck,e}$) proposed by Eurocode 6 [34] considering the brick and the mortar compressive strengths experimentally evaluated. From the analytical formulation proposed by Eurocode 6 [34], the characteristic masonry compressive strength ($f_{ck,e}$) and the elastic modulus (E_e) are obtained from the following equations:

$$f_{ck,e} = K \cdot f_b^{0.7} \cdot f_m^{0.3} \quad (3)$$

$$E_e = 1000 \cdot f_{ck,e} \quad (4)$$

where the coefficient K, the mortar compressive strength (f_m) and the compressive strength of the brick (f_b) are assumed equal to 0.44, 7.22, and 44.0 MPa, respectively. However, the experimental determination of the masonry characteristic compressive strength (namely $f_{ck,p}$) proposed by standard BS EN 1052-1:1999-[33] includes masonry specimens with vertical joints (i.e., wallets). Considering that the prisms tested do not include vertical joints (see Fig. 4) the characteristic masonry compressive strength (f_k) is derived from the formulation proposed by Thamboo et al. 2019 [35]. They found that the masonry characteristic compressive strength of specimens without vertical joints (prisms) can be considered as 75% of the wallet characteristic masonry compressive strength obtained using specimens with vertical joints. The characteristic masonry compressive strength ($f_{ck,p}=f_{c,p}$ / 1.2) obtained by prism specimens is equal to 16.3 MPa, and using the Thamboo et al. 2019 [35] correlation, it is possible to define the wallet characteristic masonry compressive strength equal to 12.2 MPa. Moreover, the analytical formulation (3) proposed by Eurocode 6 [34] evaluates a masonry characteristic compressive strength ($f_{ck,e}$) equal to 11.3 MPa, which is 7.5% lower than the wallet characteristic masonry compressive strength.

3. SFRM EXPERIMENTAL CHARACTERIZATION

The SFRM material is composed of cement, aggregates, water, superplasticizer and steel fibers (see Fig. 5.) with the proportions reported in Table 4 [19]. The steel hooked-end fibers have a length L_s=30 mm, nominal thickness t_s=0.55 mm and the mechanical properties reported in Table 5.

Fig. 5. SFRM components.

Table 4. Mix details of SFRM material

Cement	48 % v/v
Water	12 % v/v
Superplasticizer	1 % v/v
Steel fiber	2 % v/v
Aggregates (0 – 3.2 mm)	37% v/v

Table 5.Steel fiber properties

	Standard	Steel fiber length L_s [mm]	Steel fiber nominal thickness t_s [mm]	Steel fiber Elastic modulus [MPa]	Steel fiber tensile strength f_{fsu} [MPa]
Steel fiber (Hooked Ends shape)	EN-14889-1:2006	30	0.55	210000	1345

The preparation of the SFRM required a rotary mixer that contains 25 kg of the material. The cementitious matrix, the steel fibers, and water were placed in the mixer and the mixing procedure was held for two minutes At that point, the superplasticizer was added and the mixing was carried out for one more minute. During the mixture process, through visual inspection, it was possible to observe that the steel fibers were distributed homogeneously. Vibration of the specimens was not needed due to the self-compacting property of the material. In fact, when applied to existing structures, vibration of the formwork should be avoided as it can cause sedimentation/precipitation of the fibers.

3.1. Flexural and compressive strength of the SFRM mortar

The flexural and compressive strength of the SFRM mortar (i.e., without fibers) was carried out following the procedure described in section 2.1 and the results are shown in Table 6. In addition, the flexural and compressive strengths of the mortar used for SFRM were evaluated at 1, 7, 14, and 21 days after casting. Fig. 6 shows the development of the strengths in terms of the percentage of maximum strength obtained at 28 days. Results show that after seven days of casting, the evaluated mechanical properties of the mortar are about 80% of the maximum value attained at 28 days after casting.

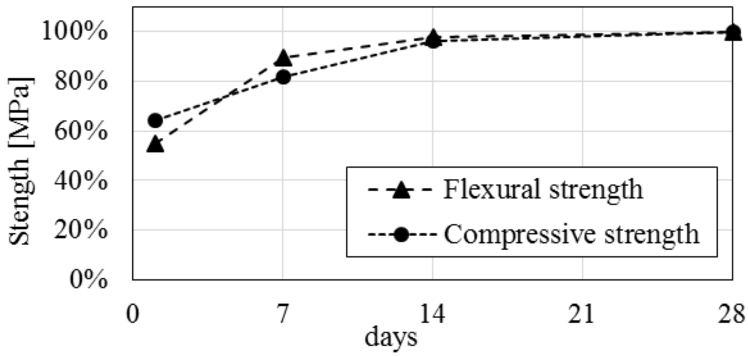

Fig. 6. SFRM mortar Strengths - days.

Table 6. SFRM mortar mechanical properties.

Material	Density	Compressive strength (f_m)		Flexural strength (f_{fm})		Elastic Modulus (E_m)	
	[kg/m^3]	[MPa]	CoV [%]	[MPa]	CoV [%]	[MPa]	CoV [%]
SFRM Mortar (28 days)	2402	91.02	1.59	15.43	11.98	24040	22.01

3.2. SFRM residual flexural tensile test

As reported in the BS EN 14651-2005 [36], steel fiber reinforced mortars can have different flexural post-elastic behavior (hardening or softening). The SFRM flexural post-elastic behavior depends on the percentage in volume of the steel fibers and it can show a hardening or a softening behavior if the fiber percentage is greater or lower than 2% (CNR-DT 204/2006 [37]), respectively. The SFRM used in this experimental campaign has a fiber volume of around 2% of mortar.

In order to evaluate the SFRM flexural behavior, three-point bending tests were carried out using specimens with dimensions 100 x100 x 500 mm and shown in Fig. 7. The specimens were cast using a formwork that was removed after 24 hours. The specimens were then covered with a plastic film for 28 days.

The test set-up used to evaluate the deflection of the specimen consists of a rigid frame with a sliding fixture ("*A*", y = 0) and a rotating fixture ("*B*", y = x = 0), as seen in Fig. 7a and Fig. 7c.

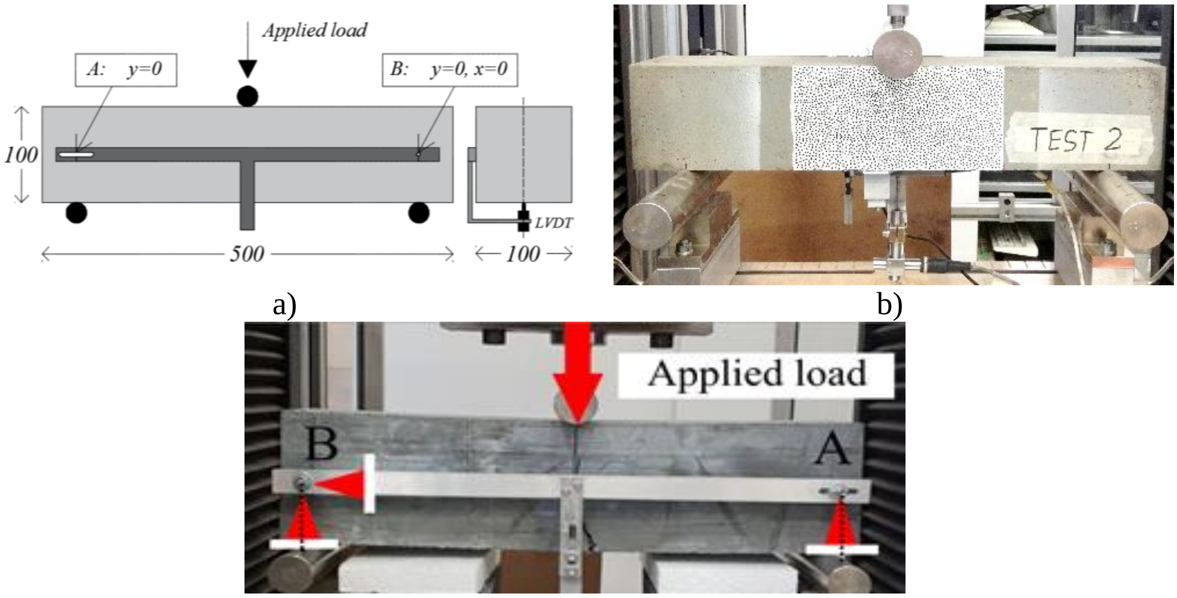

a) b) c)

Fig. 7. Residual flexural strength: a) Test setup SFRM; b) Specimen being tested. c) Specimen after testing.

In Fig. 8, the Load-Displacement curves obtained from the three tests are reported. The displacement shown in Fig. 8 corresponds to the mid-span displacement obtained using the measurement system represented in Fig. 7b. Fig. 8 also includes the typical crack witnessed at the end of the descending branch.

From the analysis of the fracture surface, it was observed that the fibers are evenly distributed and orthogonal to the fracture. It is possible to conclude that the steel fibers contributed to the flexural strength of the specimens because the behavior of SFRM is similar to that observed on similar materials with the same amount of fiber volume [19]. In addition, the fracture plane spread to the top of the specimen offering residual flexural strength. In the absence of fibers, this behavior could not be observed. Furthermore, during the test, after the maximum load is attained, it is also possible to observe in Fig.8 the presence of instantaneous load reductions with subsequent recovery, which can be associated to the rupture or debonding of the steel fibers.

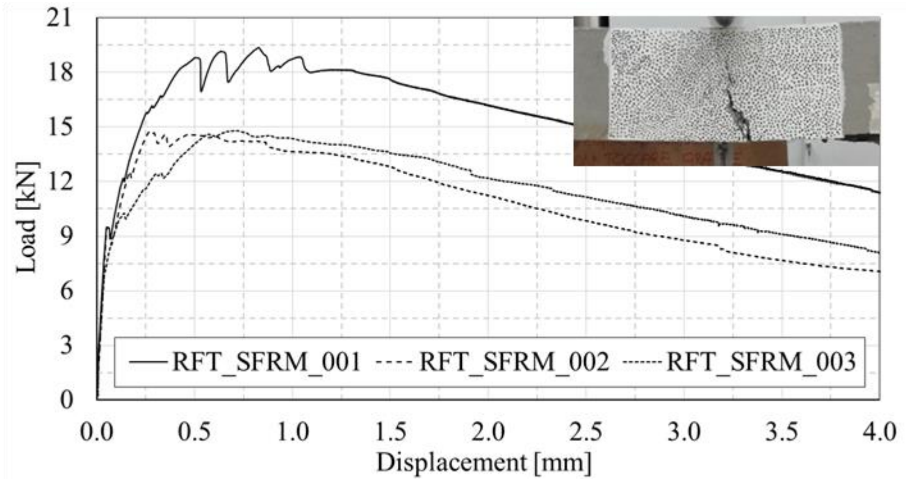

Fig. 8. Load-Displacement curves for SFRM specimens.

3.3. SFRM direct tensile test

In order to investigate the direct tensile strength of the SFRM, direct tensile tests were carried out. The specimens were cast using a formwork with the following dimensions: 500mm of height, 80 mm of width, and 30 mm of thickness. The SFRM composite material was cast considering the direction of the fibers where the principal direction coincides with the direction of the applied load. After casting, the specimens were covered with a plastic film in order to maintain the humidity constant for 28 days and tested using a non-standard test setup showed in Fig. 9.

The SFRM specimens were anchored on both sides with steel plates. Epoxy resin was applied between the specimen and the steel plates to avoid any slip phenomenon (Fig. 9a). The tensile force was applied to the specimen through two articulated joints that avoid the presence of bending moments in the SFRM strip during testing (Fig. 9b). Two LVDTs placed at the middle height of the lateral sides of the specimen were used to investigate the strain of the SFRM strip (Fig. 9a-b). The measuring length of the instruments is equal to 100 mm.

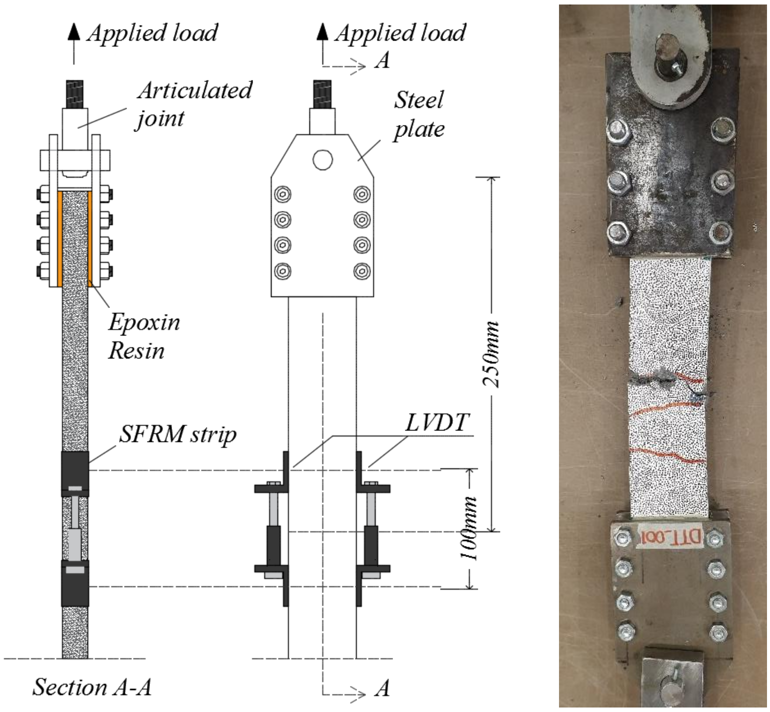

a) b) c)

Fig. 9. Direct tensile test: a) Anchorage system with epoxyn resin and steel plates; b) testing setup, c) failure mode.

In Fig. 10 the stress-strain curves of the five direct tensile experimental tests carried out are reported. To obtain the stress-strain curves, only the specimens which shown a fracture within the gage length (equal to 100 mm as shown in Fig. 9) were considered. The material shows a first elastic branch on the stress-strain curve due to the matrix and steel fibers working together. After the peak of stress is attained, the subsequent strain is due only to the tensile steel fiber strength. As a simplification, the stress is calculated considering the entire section area instead of the steel fiber. The mean stress peak value of the direct tensile test corresponds to 3.98 MPa (see Table 7) with a strain of around 0.078%.

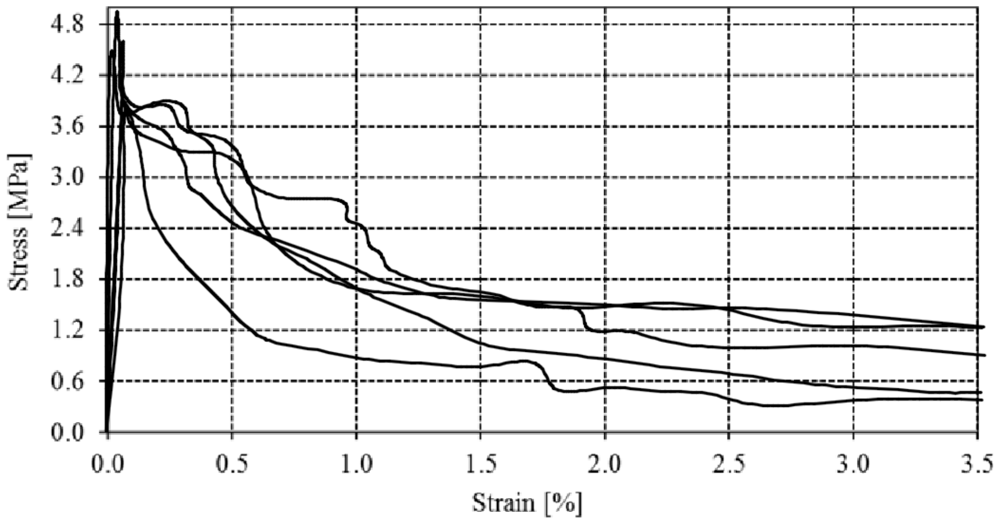

Fig. 10. Stress-Strain curves derived from direct tensile tests.

Table 7. SFRM direct tensile test.

Specimen	Tensile strength		Corresponding Strain	
	[MPa]	CoV [%]	[%]	CoV [%]
DTT_SFRM_001	3.43		0.0781	
DTT_SFRM_002	4.15		0.0861	
DTT_SFRM_003	3.08		0.0612	
DTT_SFRM_004	3.83		0.0793	
DTT_SFRM_005	4.51		0.0862	
Mean value	3.98	14.23	0.0782	13.05

3.4. Smooth and simplified tensile strength curves

The mean smooth stress-strain curve derived from direct tensile tests is compared with the simplified mean curve obtained from the analysis of the residual flexural tensile test results (Fig. 11). The average tensile stress-strain curve derived from the results of the residual flexural tests was evaluated according to the BS EN 14651-2005 [36] and it is shown in Fig. 11. This curve also includes values of tensile strength f_{Ft}, serviceability tensile residual strength f_{Fts}, and ultimate tensile residual strength f_{Ftu} (see Table 8). As can be seen in Fig. 11, the first and third points of that curve are closer to the direct tensile stress-strain curve than the second point.

Finally, it is important to underline that the SFRM material shows a tensile strength reduction around 50% after a large strain (around 1%).

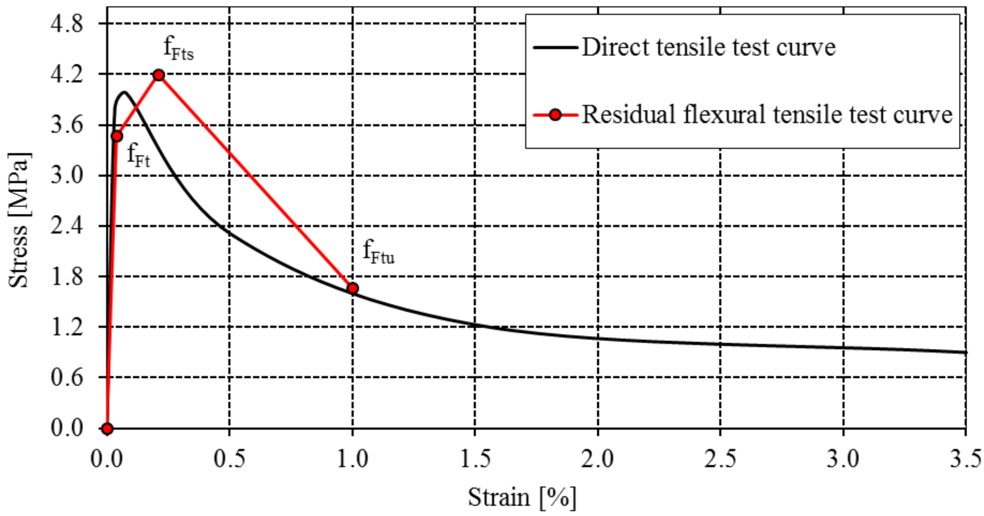

Fig. 11. Stress-Strain smooth mean curves derived from direct tensile tests and residual flexural tensile tests.

Table 8. SFRM Residual flexural strength test results.

Material	f_{Ft}		f_{Fts}		f_{Ftu}	
	[MPa]	CoV [%]	[MPa]	CoV [%]	[MPa]	CoV [%]
RFT_SFRM_001	3.79		4.82		2.28	
RFT_SFRM_002	3.79		3.93		1.14	
RFT_SFRM_003	2.81		3.84		1.58	
	3.46	16.34	4.20	12.91	1.66	34.49

As can be seen in Table 8, the dispersion of the results (tensile strength f_{Ft}, serviceability tensile residual strength f_{Fts}, and ultimate tensile residual strength f_{Ftu}) carried out from the three points bending tests (according to the BS EN 14651-2005 [36]) is quite high with respect to the CoV obtained from the masonry mortar tests (Table 6). This result depends on the randomness of the SFRM materials that is a consequence of the random distribution of the steel fibers within the mortar matrix [38, 39].

4. SFRM-MASONRY BOND BEHAVIOR

The results reported in section 3 show the SFRM material has high compressive and tensile strength with respect to a masonry material and shows a ductile tensile behavior. The effectiveness of this strengthening system is intrinsically dependent on the bond performance between the SFRM material and the masonry substrate and this issue requires further investigation.

Considering a masonry cross-section with a bottom or a top layer of SFRM strengthening, the bond actions depend on the type of forces applied to the SFRM and on the curvature of the masonry element. In general, such bond actions are tangential (i.e., shear) and normal stresses applied at the masonry-SFRM interface [40]. In this experimental campaign, double shear lap tests were performed in order to investigate the existence of an effective bond length *(L_b)*, the failure mode, and the shear bond stress developed at the masonry-SFRM- interface. Due to the test set-up, the presence of normal stresses is not expected.

In this article, the effective bonded length *(L_b)* is defined as it has been reported for other types of composites externally bonded to concrete or masonry (concrete structures strengthened with FRP [40, 41], FRCM [42-44], and masonry structures strengthened with FRP [45, 46], FRCM [47-49]. The double shear lap tests performed in this experimental campaign were developed using the specimens shown in Fig. 12.

Fig. 12. Double shear lap test specimens.

Considering a strip of SFRM with bonded width (b) and bonded length (L), the effective bonded length (L_b) can be defined as a length where the forces in the SFRM strip are transferred to the masonry substrate through shear stresses in the interface between two materials. If the bonded length is greater than L_b the composite material is able to transfer the maximum load to the masonry. This maximum load, as will be shown in the following, depends on the shear failure mode of the bonded material.

The specimens were prepared in three different phases. First, two masonry prisms were made over a horizontal steel plane parallel to the mortar joints. Then, a timber element was used to keep the two prisms 100 mm apart (Figure 13a). A protection film was applied to the specimens' surface, with the exception of the bonded area. In this way, the area in which the SFRM strip was applied was delimited. Two formworks were built and then positioned laterally as shown in Figure 13. The thickness of the SFRM strip was guaranteed by means of hard rubber elements with a thickness of 30 mm located between the wood formwork and the specimen. The SFRM matrix was then cast and the formworks were removed after 14 days. The tests were performed after 28 days of casting. The application of the SFRM to the masonry substrate was carried out without any previous surface preparation as former experimental evidence [24] demonstrated that an adequate bond between the SFRM and the substrate was obtained in that condition.

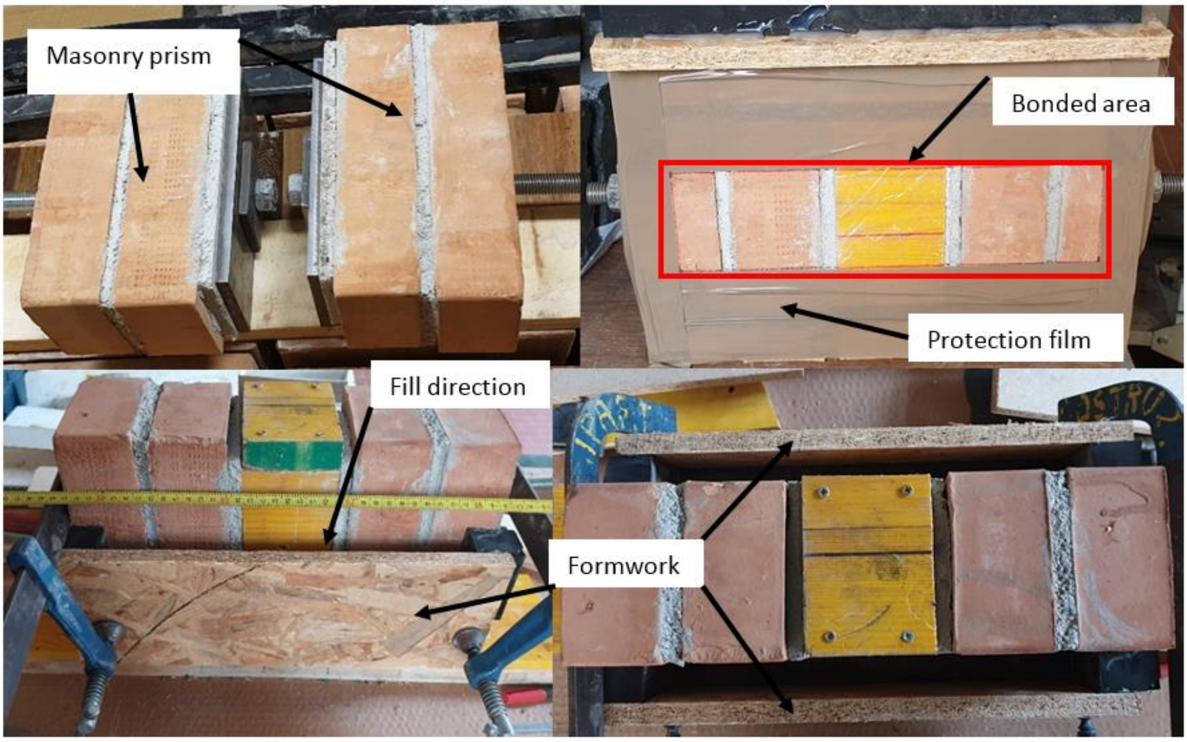

Fig. 13. Double shear lap test specimens' preparation.

The two-masonry prisms, connected by two SFRM strips placed on the two sides of the masonry element, have a hole (Fig. 13) where a steel bar is inserted and connected to a steel plate at the bottom of the masonry specimen (Fig. 13). In this manner, it is possible to apply the load as a pressure to the steel plate connected to the steel bar and then to the masonry specimen (Fig. 14). The test was conducted in displacement control defined with a rate equal to 0.5 mm/min. Four LVDTs were used to define the displacement between the two ends of the masonry prisms, as can be seen in Fig. 12. The LVDTs record the variation of the distance *c* with the application of the imposed displacement. In addition, five strain gauges were applied to the middle thickness of the strip in order to evaluate the variation of strain along with the composite layer for each value of imposed displacement (see Fig. 14a).

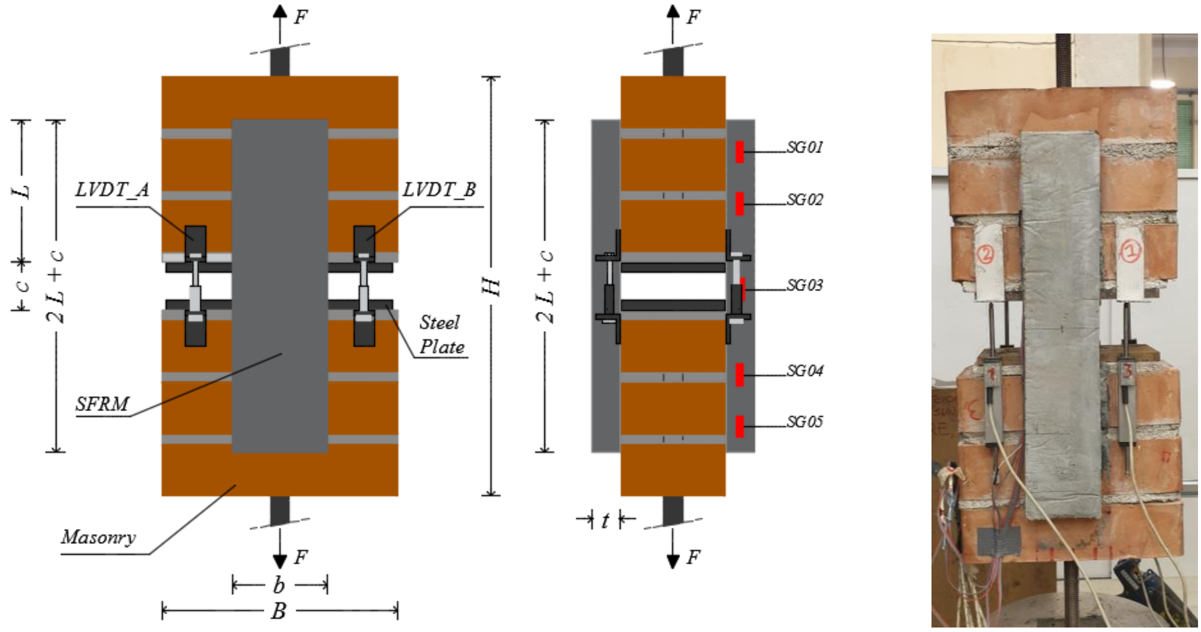

Fig. 14. Double shear lap tests: a) Test setup, b) specimen being tested.

The SFRM strip has 30 mm of thickness (*t*) and 80 mm of width (*b*), and two different bond lengths (*L*) are considered (100 mm and 150 mm). The entire specimen has 540 mm of total height (*H*), and the distance (*c*) between the masonry triplets connected with SFRM strip is 100 mm. The masonry specimens have a cross-section equal to the brick dimensions (245 mm x 110 mm). The tests are named following the convention *DSL_SFRM_X_Z* where DSL represents the test type considered (double shear lap test), SFRM is referred to the composite material investigated, *X* is the bonded length considered, and *Z* is the numbering of the test. For the bonded lengths (*L*) 100 mm and 150 mm three and six specimens were tested, respectively. In Table 9, the values of maximum load attained during testing (F_{max}), the maximum global shear stress ($\tau_{g,max}=F_{max}/(2\cdot L\cdot b)$) and the failure mode observed for each test are reported.

Three failure modes were observed (see Fig. 15): *D*, detachment of the SFRM strip ~~to~~ the masonry substrate (Fig. 15a); *C*, cracking of the SFRM strip (Fig. 15b); and *CD*, cracking of the SFRM with cracks that running parallel to the interface and SFRM detachment (Fig. 15c).

Table 9. SFRM Double shear lap test

Specimen	L [mm]	F_{max} [kN]	$\tau_{g,max}$ [MPa]	Failure mode
DSL_SFRM_100_001	100	9.01	0.56	*D*
DSL_SFRM_100_002	100	10.50	0.66	*D*
DSL_SFRM_100_003	100	12.13	0.76	*D*
DSL_SFRM_150_001	150	18.14	0.76	*C*
DSL_SFRM_150_002	150	7.67	0.32	*D*
DSL_SFRM_150_003	150	19.86	0.83	*CD*
DSL_SFRM_150_004	150	17.85	0.74	*C*
DSL_SFRM_150_005	150	17.93	0.75	*C*
DSL_SFRM_150_006	150	19.72	0.82	*C*

Experimental results show that the bonded length of 100 mm is insufficient to develop the shear stress necessary to guarantee the transfer of the maximum force from the SFRM to the masonry substrate. In fact, the average value of the maximum global shear stress ($\tau_{g,max}$) reached for 100 mm bond length is equal to 0.66 MPa (Table 9) which is lower than the value obtained from the tests with 150 mm of bond length (0.78 MPa). With this last bonded length, the specimens showed cracking failure, and a perfect shear stress transfer was observed (with the exclusion of specimen *DSL_SFRM_150_002* that shows an early detachment). The mean maximum load reached for the specimens with L=150mm (with exclusion of *DSL_SFRM_150_002*) is equal to 18.70 kN. The corresponding average normal stress in the strip cross-section is equal to 3.89 MPa which is only 2.2% lower than the average tensile strength (evaluated by direct tensile tests and reported in Table 7). This result means that if the bonded length is equal to or greater than effective bonded length, there is a perfect force transfer from SFRM to masonry because the observed failure mode involves in the tensile rupture of the strengthening and detachment is not observed (Fig. 15).

4.1. Shear lap test failure modes

The failure mode registered for the bonded length equal to 100 mm is the detachment of the SFRM strip from the masonry substrate (Failure mode "*D*"), as shown in Fig. 15a. Therefore, the bonded length of 100 mm is considered insufficient to have the perfect transfer of the stress from SFRM to masonry.

For the bonded length equal to 150 mm, results show three different failure modes: four specimens show cracking of SFRM in the unbonded region until the tensile rupture of the SFRM without detachment of the composite from the substrate (Failure mode "*C*", Fig. 15b); one specimen (test DSL_SFRM_150_003) shows cracking along the SFRM strip in the bonded and unbonded area cracks until the detachment of the composite material from the masonry (Failure mode "*CD*", Fig. 15c); one specimen (test DSL_SFRM_150_002) shows an early detachment of the SFRM from the masonry (Failure mode "*D*" , Fig.15a).

Test DSL_SFRM_150_002 was not considered in the results analysis because it showed an early detachment corresponding to an applied load of 7.67 kN (see Table 6) which is lower than the average maximum load (18.70 kN) registered for the other specimens with L=150 mm. This could be justified because after a visual inspection of the specimen, it was observed that the strip surface was not completely bonded to the masonry surface. In addition, the reason for the type of failure witnessed for specimen DSL_SFRM_150_002 can also be attributed to a small misalignment (i.e., eccentricity with respect to the machine axis) of the sample that might have caused a concentration of stresses on one of the strips causing its earlier detachment.

Test DSL_SFRM_150_003 reached a maximum load (19.86 kN, see Table 9) which is similar to the results obtained for the remaining specimens, even if it shows a different failure mode (see Table 9).

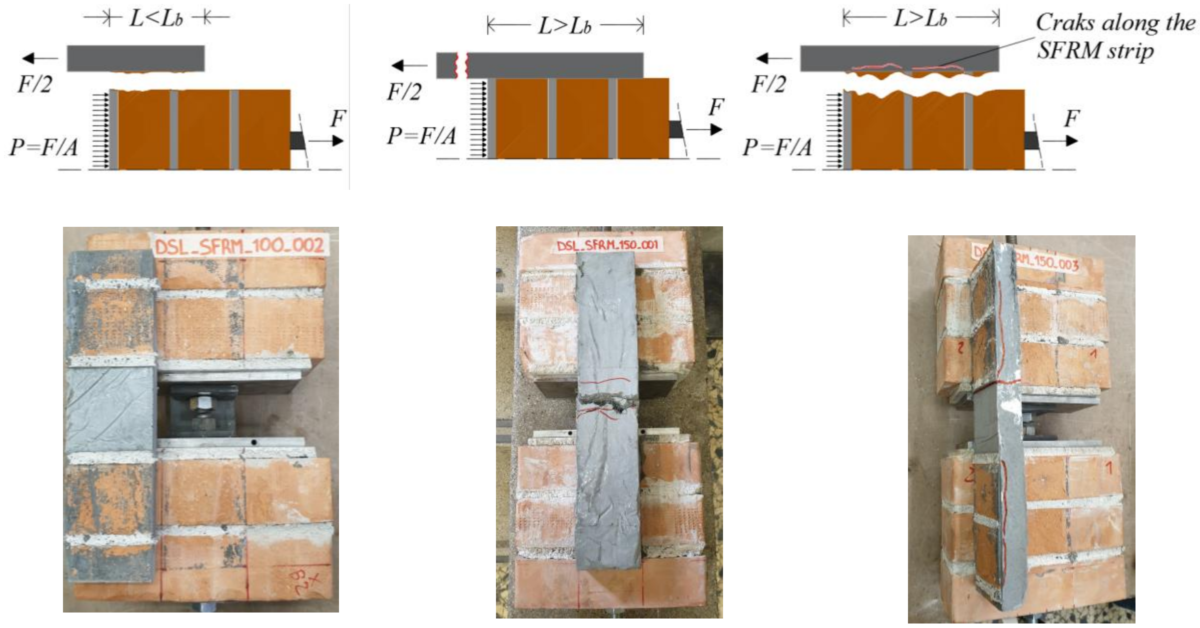

a) b) c)

Fig. 15. Failure modes obtained from the double shear lap tests: a) DSL_SFRM_100 failure mode "*D*"; b) DSL_SFRM_150_ (001, 004, 005, 006) failure mode "*C*"; c) DSL_SFRM_150_003 failure mode "*CD*".

4.2. Shear lap test behavior

In Fig. 16a, the Applied load in the strip (*F/2)*–Displacement diagram obtained from all the double shear tests are reported. The displacement evaluated during the experimental test represents the variation of the distance (*c*) between the two masonry prisms ends that in the unloaded condition is equal to 100 mm (see Fig. 16a). The tests with *L*=100 mm were stopped after the detachment of SFRM (Fig. 16a). Tests with *L*=150 mm show an initial elastic branch before the cracking of SFRM (see Fig. 16a). Then, a non-linear branch, similar to that witnessed during the direct tensile tests and reported in Fig. 10, is observed. In Fig. 16b the Applied load -Global slip curves are presented until the failure mode. The slip value reported in Fig. 16b is equal to half of the mean displacement evaluated by LVDTs minus the SFRM strip elongation (evaluated considering the strain registered by the strain gauge in the middle of the strip).

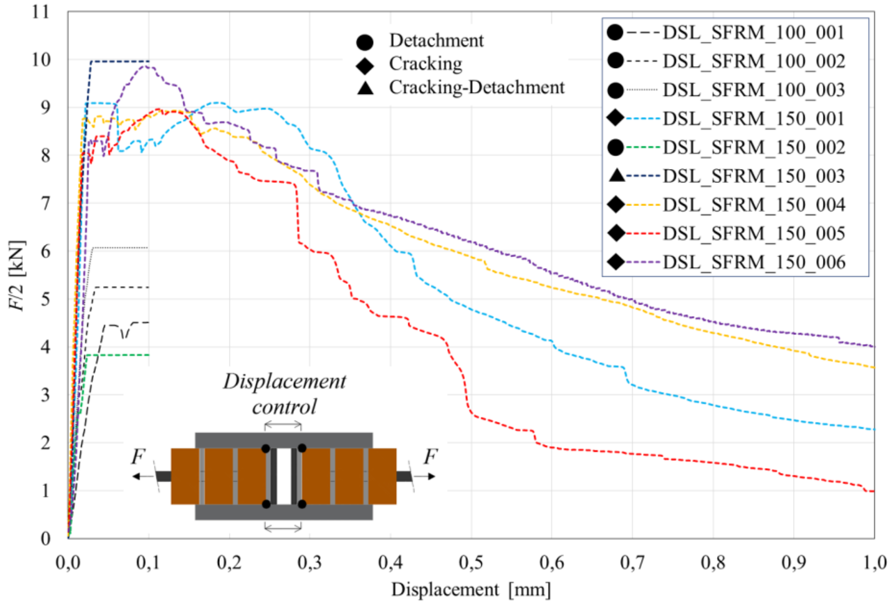

a)

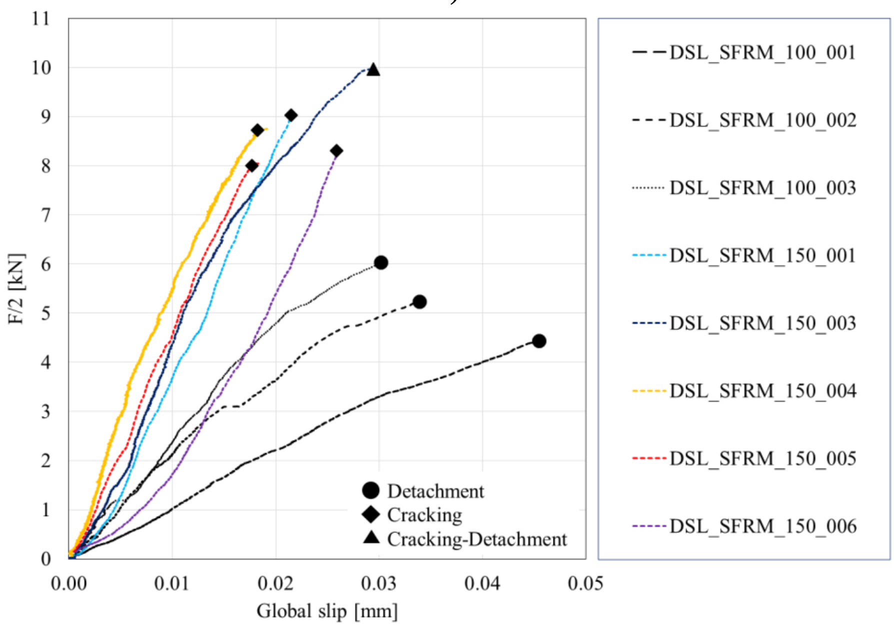

b)

Fig. 16. Double shear lap test results: Applied load - Displacement diagrams a) Entire experimental curves b) Load-Global slip curve until specimen failure.

Results in Fig. 16b show that the curves with (*C*) failure mode present a mean global slip of around 0.022 mm while the (*D*) failure mode of around 0.037 mm. In Fig.16b, it is possible to see that specimens with 150 mm of bonded length have a higher initial stiffness compared to that of specimens with 100 mm of bonded length, i.e., specimens with 100 mm of bonded length show higher global slip displacements for the same amount of applied load when compared to specimens with 150 mm of bonded length. This behavior is explained when it is considered that for specimens with lower values of bonded length, the tangential stress reaches its maximum value for a lower applied load, and the global slip increases more rapidly.

4.3. Stress – Strain development along the SFRM strip

Five strain gauges were used with the aim to determinate the strain distribution along the bond length of the SFRM strip during tests DSL_SFRM_150 (001, 003, 004, 005, and 006). The strain gauges were applied to the middle thickness of the strip (Fig. 17): one at the middle span of the strip (SG03), SG02 and SG01 were respectively applied at L_1 (110 mm) and at L_1+L_2 (170 mm) from the SG03. SG04 and SG05 were applied in the symmetrical position with respect to SG02 and SG01.

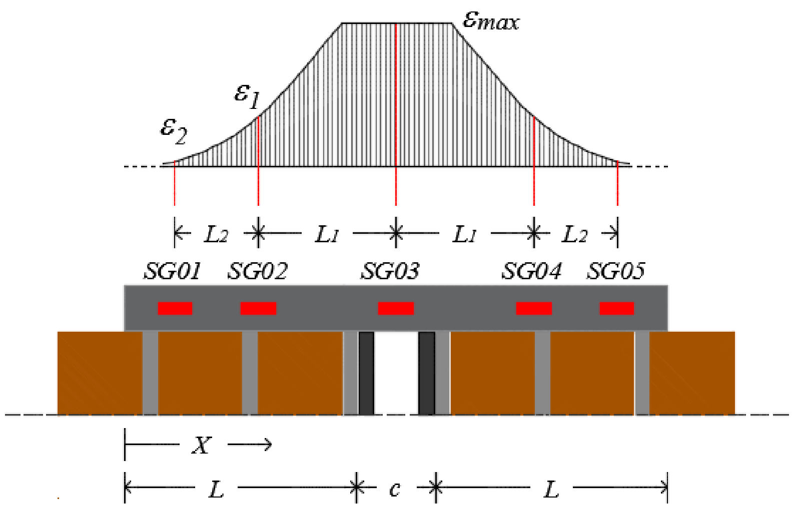

Fig. 17. Disposition of the strain gauges used in tests DLS_SFRM_150.

The results in terms of strain from tests with a bonded length (L) equal to 150 mm are reported in Fig. 18. The strain distribution from test DSL_SFRM_150_002 was not included since results from this test were disregarded. The strain values (ε_i) at the maximum load reached during the experimental test are normalized with respect to the maximum strain (ε_{max}) reached in the middle of the strip of the corresponding test.

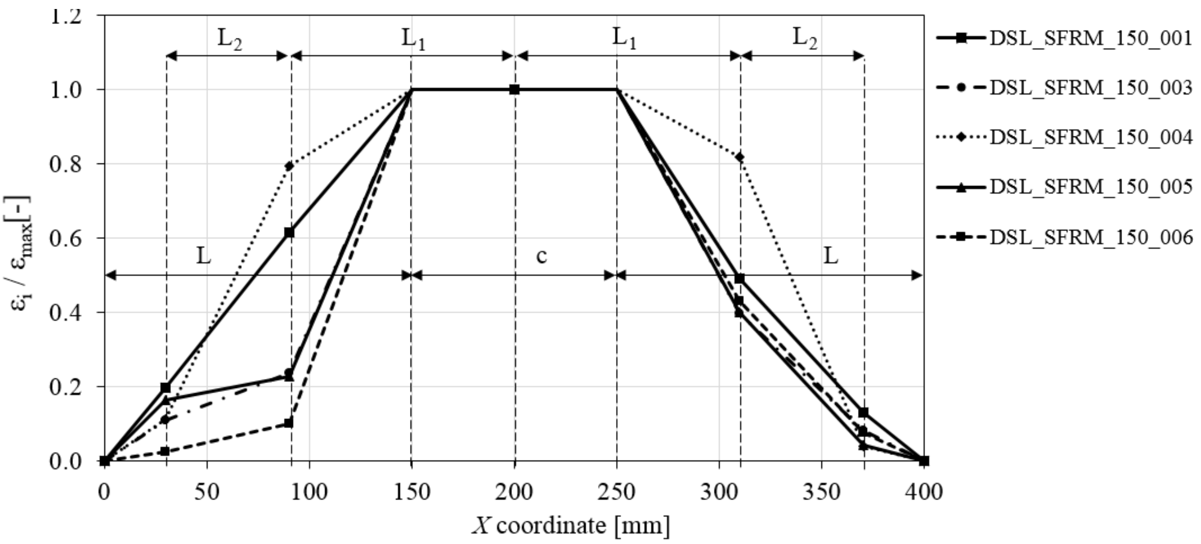

Fig. 18. Normalized strain distribution carried out from the DSL_SFRM_150 tests.

As it can be seen in Fig. 18, maximum values of the strain are observed in the unbonded region and decrease to the bonded strip ends.

5. NUMERICAL CALIBRATION

In this section, a detailed numerical investigation is presented with the aim of simulating the experimental results described above. Numerical analyses were developed through finite element models considering the non-linear behavior of the materials. In the following, the different numerical strategies used to reproduce the compressive tests of the masonry prism, the SFRM tensile tests, and the double shear lap tests are discussed.

The numerical model were made using CQ16M 2D plane stress elements. This type of elements were used for the masonry mesh and also for the SFRM material mesh. The quadratic interpolation and Gauss integration type were adopted for the eight-node quadrilateral isoperimetric plane stress elements. The nonlinear system was solved with iteration type and for the iteration scheme a modified Newton-Raphson algorithm with 0.01 energy norm was used. The elements have an average area of around 250mm^2 (with the exclusion of the elements used for the discretization of the masonry mortar joints reported in Fig. 19a).

The FE model used in the numerical analysis is mesh depending. For this reason, different numerical models with different mesh sizes were developed with the aim of obtaining reliable results. The mesh dimension was chosen considering a compromise between a good agreement with the experimental test and computational time. Moreover, the average mesh dimension was calibrated on the base of experimental test results in order to avoid results localizations [50].

The masonry compressive tests were numerically studied considering the simplified micro-modelling approach shown in Fig. 19a where mortar and bricks were separately discretized and the "Total Strain Crack Model" (TSCM) was used as non-linear constitutive law of the materials. Parabolic stress-strain diagrams (see Fig. 20a) were used to consider the compressive behavior of mortar and bricks and linear elastic with exponential softening laws (Fig. 20b) were used for modelling the tensile behavior of the materials.

These stress-strain relationships, shown in Fig. 20b, were defined according to the parameters in Table 10: Elastic Modulus (E), material compressive strength (f_c), material tensile strength (f_t), compressive fracture energy (G_{fc}) and tensile fracture energy (G_{ft}). Results from the simplified micro-modelling approach were compared with the experimental results and with those of a macro-modelling approach (Fig. 19b) where masonry was considering as continuum material.

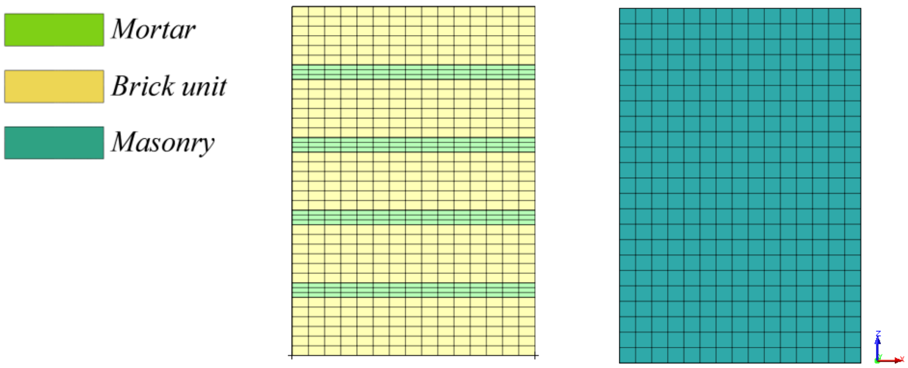

a) b)

Fig. 19. Masonry prism models: a) simplified micro-modelling approach; b) macro-modelling approach.

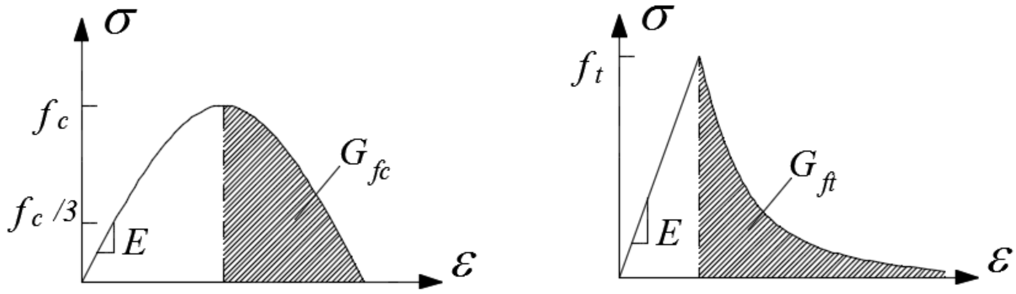

a) b)

Fig. 20. Stress-strain curves used for the numerical analysis a) parabolic function; b) linear with exponential softening function.

Table 10. Material mechanical properties of masonry numerical models.

			Compression			Tension		
Material	Density [kg/m^3]	E [MPa]	f_c [MPa]	G_{fc} [N/mm]	Function type	f_t [MPa]	G_{ft} [N/mm]	Function Type
Brick unit	1700	8700	44.0	8	parabolic	3.00	0.01	exponential
Masonry joint mortar	1770	3700	7.22	8	parabolic	2.22	0.01	exponential
Masonry	1714	7500	19.5	-	parabolic	4.06	3.00	exponential
SFRM matrix mortar	2400	24000	91.0	-	E-P	3.6	9.00	exponential

From Fig. 21, it is possible to observe that the initial stiffness corresponding to the elastic branch is similar for the micro and macro model curves and those obtained experimentally. In addition, the macro model shows a descending branch more ductile respect to the micro model.

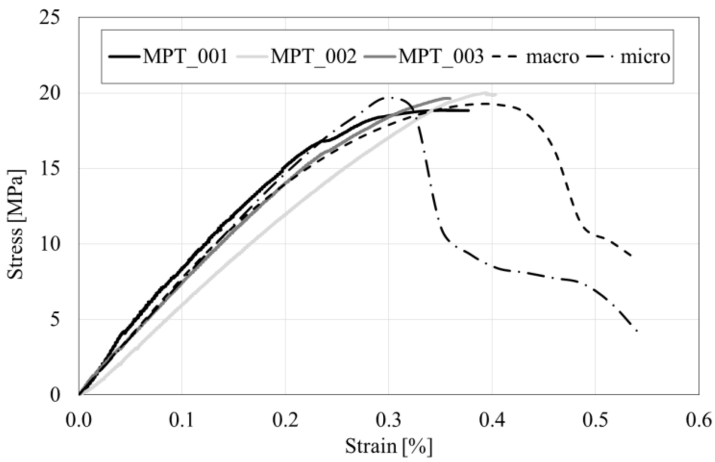

Fig. 21. Stress strain result of the masonry prisms, numerical analysis - experimental test results.

The SFRM was discretized with finite elements (Fig. 22a) and its tensile stress-strain curve (assumed in the TCSM) was calibrated considering a linear elastic branch with an exponential softening curve (Fig. 20b). The tensile fracture energy (G_{ft}=*9 N/mm*, Table 10) was calibrated in order to obtain a good correspondence between numerical and experimental stress-strain curves of the tensile behavior of SFRM strip as reported in Fig. 22b. This calibration analysis has considered a strain range between 0% and 1% that is defined from the stress-strain reported in Fig. 8 and obtained from residual flexural tests. The SFRM compressive stress-strain law used is an elasto perfectly plastic (E-P) curve defined considering the experimental values of the elastic modulus and the compressive strength (E and f_c) reported in Table 10.

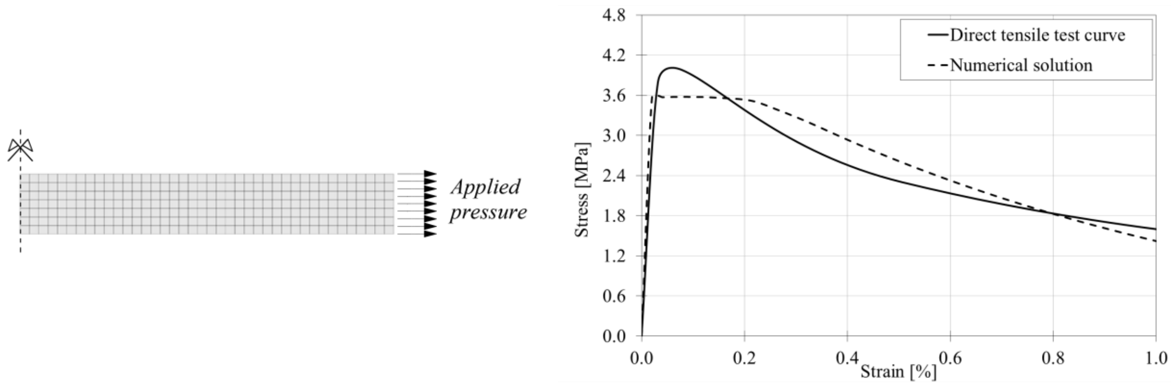

a) b)

Fig. 22. Tensile tests modelling: a) Discretization of SFRM material with finite elements; b) Stress - Strain result for the numerical solution compared with the direct tensile test curve (experimental).

Lastly, the bond behavior between SFRM and the masonry substrate was investigated using the finite element model illustrated in Fig. 23a. Fig. 23a shows the mesh used, the boundary conditions (Fig. 23b) and local stress ($\tau(s)$)-slip (s) curve implemented in the bond-slip interface type inserted between masonry and SFRM composite material (Fig. 23c). In the bond-slip interface, a local tangential tress $\tau(s)$-slip (s) curve to calibrate the parameter of the well-known equation proposed by Popovics et al. 1973 [51] was implemented:

$$\tau(s) = \tau_{max} \frac{s_p}{\bar{s}} \frac{n}{(n-1)+\left(\frac{s}{\bar{s}}\right)^n} \quad (5)$$

where the ultimate slip s_u is equal to 0.4 mm (according to CNR-DT 200 R1/2013 [52]), $\bar{s}$ (0.022 mm) is the slip corresponding to the peak value of the tangential stress (τ_{max}=1.9 N/mm^2), finally the factor n in equation (5) is assumed equal to 3.

The interface element between SFRM and masonry has zero thickness [53] and the slip zone was described with a bond-slip interface model, which has a constitutive law based on the "Total Deformation Theory" [54]. This theory expresses the bond strength as a function of the relative tangential displacement (s) between the two materials. The normal tension (t_n) parameter was considered rigid, while the relationship between the tangential stress (τ) and the relative tangential displacement is assumed to be non-linear (Figure 22).

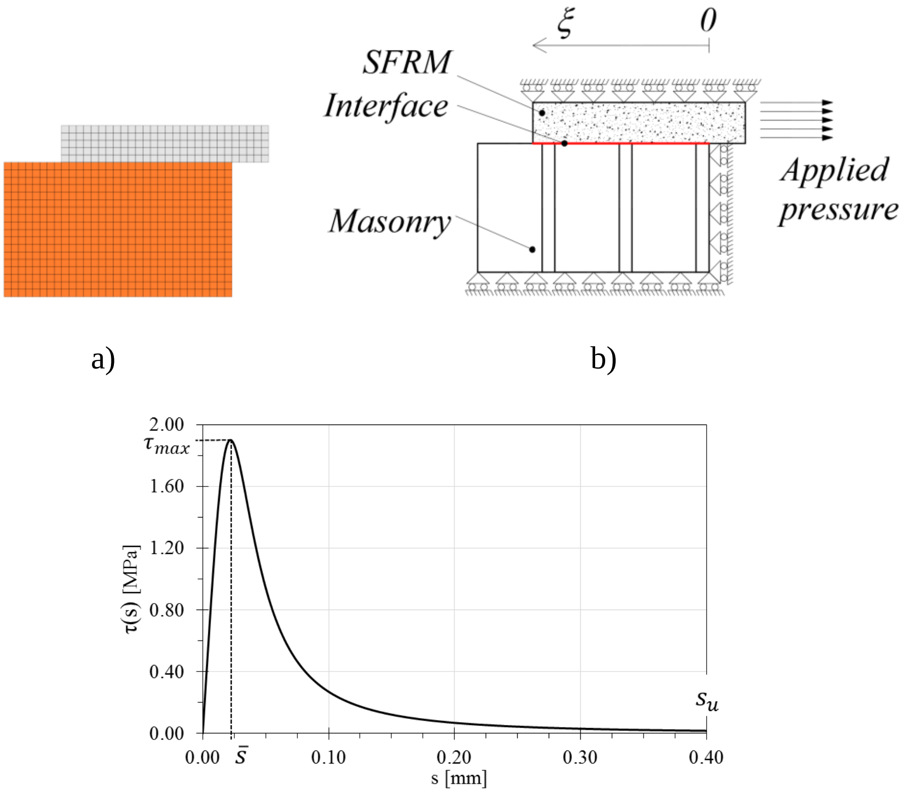

Fig. 23. a) Shear lap test model b) Boundary conditions and load applied to the F.E. model c) Local bond–slip curve implemented in the bond-slip interface element.

Fig. 24 shows the dimensionless strain ε_i / ε_{max} in the middle thickness of the SFRM strip as a function of the coordinate ξ (from 0 mm to 150 mm). The numerical results obtained considering a bonded length (L) equal to 100 mm and 150 mm were compared with those obtained from the strain gauges used in the DSL_SFRM_150 experimental tests (Fig. 24). The dimensionless normal strain is maximum when for $\xi = 0$ and is equal to zero for $\xi \geq L_b$ as reported in Fig. 24. The numerical simulation confirms that L=100 mm is lower than the bonded length because for $\xi = 100\ mm$ strain is different from zero. Moreover, it is possible to see from Fig. 24 that the numerical strain distribution is comparable to the experimental one.

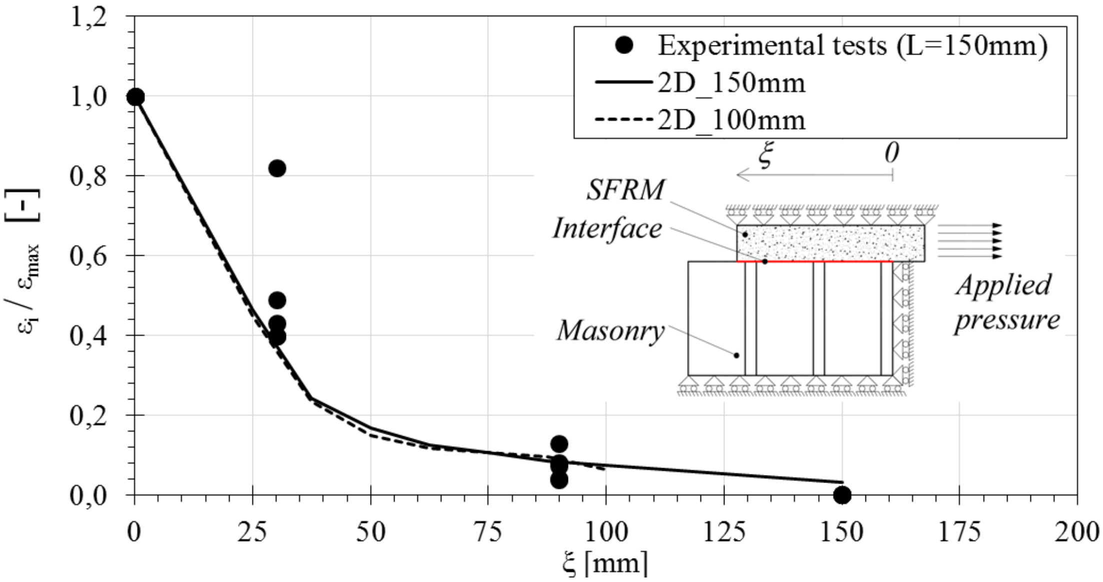

Fig. 24. Dimensionless strain – ξ coordinate. Experimental and numerical results.

The load – global slip curves have been compared with the numerical simulation results until 0.05 mm of global slip. Fig. 25 shows the experimental envelope for the tests with bonded length equal to 150 mm, without considering the test DSL_SFRM_150_002. The numerical simulation has a good agreement with the envelope of experimental results. The value of the maximum load obtained from the numerical analysis was equal to 10.73 kN while the average maximum load for the experimental tests was 9.35 kN.

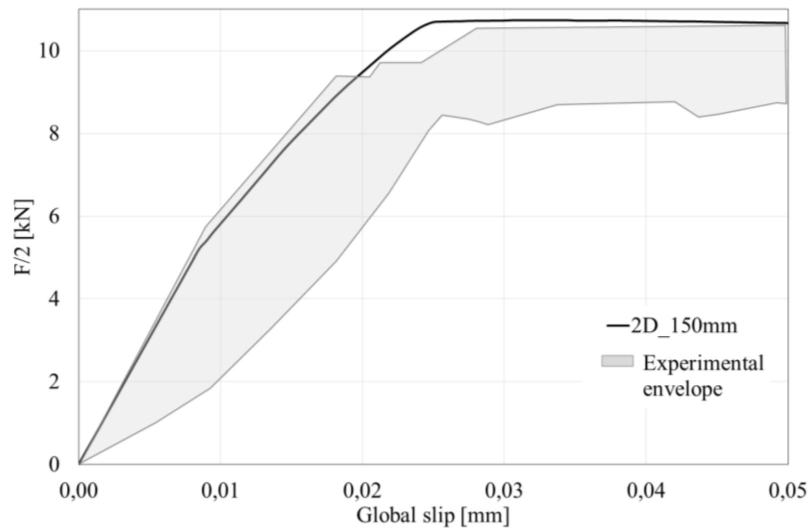

Fig. 25. Load – global slip curves Experimental envelope - Numerical results (2D_150mm)

6. FURTHER DEVELOPMENTS

The results presented in this paper corresponds to a first attempt to gain knowledge on the bond behavior of SFRM composites applied onto masonry substrates but need to be validated when more experimental data become available, as they are strictly related to the mechanical and geometric properties of the specimens tested. These results are intended to provide tools for future practical applications of the material as strengthening system and to help researchers to plan future experimental tests that focus on variables not studied here.

For instance, the presence of a bonded length, as demonstrated by the shear lap tests, implies that the system can be applied to structural members with limited size. However, aspects such a possible size effect and the influence of the thickness and width of the strips on the expected values of effective bonded length need to be considered and investigated.

It is also worth noting that the most common type of failure mode observed for specimens with bonded length equal to 150 mm (i.e., cracking of the SFRM strip without detachment) suggests that the behavior of the material might be independent of the type of substrates onto which it is applied. In this case, however, it is important to verify how the state of conservation of the masonry or its strength will affect the final behavior.

Another interesting outcome of this work is related to the fact that it was possible to achieve the maximum tensile strength of the SFRM when it was applied onto a masonry surface without any previous preparation. These results suggest that a perfect bond between the two materials might be achieved even without the need of additional application procedures. From the point of view of the practical application of the SFRM as strengthening system, this characteristic of the material will significantly reduce its cost and time of application. However, future research on the topic should validate this finding by means of tests that investigate the effect that the surface substrate characteristics (age, irregularities, etc.) might have on the bond behavior between masonry and SFRM.

Finally, it is also hoped that the information included in this paper, that comprises the characterization of all the materials involved will allow researchers to plan their experimental campaigns based on the preliminary numerical analysis carried out using the parameters herein presented.

Is also important to underline that, considering a masonry cross-section with a bottom or a top layer of SFRM strengthening, the bond actions depend on the type of forces applied to the SFRM and on the curvature of the masonry element. In general, the bond actions are tangential and normal stresses applied at the masonry-SFRM interface.

7. CONCLUSIONS

In this paper, the behavior of steel fiber reinforced mortar (SFRM) strips applied onto masonry substrates was studied experimentally and numerically with the aim of gaining insight on the behavior of masonry structures strengthened with SFRM composites. In addition, a mechanical characterization of the material was performed. Mechanical properties studied included compressive, tensile, and residual flexural strength. The main conclusions that can be drawn from this study are as follows:

- Evolution of the compressive strength of the high-performance mortar used in SFRM shows that after 7 days, the compressive and flexural strength of the matrix attained is around 80% of that witnessed after 28 days of casting.
- Comparison of tensile stress-strain curves obtained from the direct tensile and residual tensile test performed on SFRM showed a similar behavior, with an initial elastic branch followed by a softening behavior after peak stress.
- The bond behavior between the masonry substrate and SFRM composite, investigated through double shear lap tests, showed three different failure modes: detachment of the SFRM strip from the masonry substrate; cracking of the SFRM strip; and a combination of both, depending on the used bonded length. Detachment from the substrate was observed for specimens with a bonded length equal to 100 mm, while for bonded lengths equal to 150 mm, cracking of the strip with or without detachment was witnessed.
- For a bonded length equal to 150 mm, values of the maximum applied load obtained during the shear lap tests are similar to those attained on direct tensile tests. This result and the observed failure mode suggest that 150 mm can be considered as the effective bonded length for the SFRM composite studied in this paper, as a full exploitation of the material is reached.
- The strain profile along the length of the SFRM strip, at the maximum applied load, for specimens with bonded length equal to 150 mm, shows that maximum values of strain are observed at the middle of the strip (unbonded area). An exponential decrease in the strain is then observed, with values close to zero reached at the end of the strip.
- The comparison between experimental and numerical shear lap test results show that the strain profile along the SFRM strip obtained from the numerical simulations is similar to the observed experimental behavior.

8. CONFLICT OF INTEREST STATEMENT

The authors declare that there is not conflict of interest

9. ROLE OF THE FUNDING SOURCE

This research was not supported by funding source

10. ETHICAL APPROVAL

The authors approve the ethical aims of the journal

11. ACKNOWLEDGEMENTS

Eng. P. Napolitano and Mr. L. Martin are gratefully acknowledged for providing the SFRM composite material.

REFERENCES

[1] Gunes B, Cosgun T, Sayin B, Ceylan O. Structural rehabilitation of a middle byzantine ruin and the masonry building constructed above the ruin. Part II : The building. Engineering. Failure Analisys 2019; 105:527–544. https://doi.org/10.1016/j.engfailanal.2019.06.096.

[2] Caporale A, Feo L, Luciano R. Limit analysis of FRP strengthened masonry arches via nonlinear and linear programming. Compos. Part B 2012; 43(2):439–446. https://doi.org/10.1016/j.compositesb.2011.05.019.

[3] Capani F, D'Ambrisi A, De Stefano M, Focacci F, Luciano R, Nudo R, Penna R. Experimental investigation on cyclic response of RC elements repaired by CFRP external reinforcing systems. Compos. Part B 2017; 112:290–299. https://doi.org/10.1016/j.compositesb.2016.12.053.

[4] Caporale A, Feo L, Luciano R, Penna R. Numerical collapse load of multi-span masonry arch structures with FRP reinforcement. Compos. Part B 2013; 54:71–84. https://doi.org/10.1016/j.compositesb.2013.04.042.

[5] Carozzi FG, Poggi C, Bertolesi E, Milani G. Ancient masonry arches and vaults strengthened with TRM , SRG and FRP composites : Experimental evaluation. Compos. Struct. 2018; 187:466–480. https://doi.org/10.1016/j.compstruct.2017.12.075.

[6] Feo L, Luciano R, Misseri G, Rovero L. Irregular stone masonries : Analysis and strengthening with glass fibre reinforced composites. Compos. Part B 2016; 92:84–93. https://doi.org/10.1016/j.compositesb.2016.02.038.

[7] Alecci V, Focacci F, Rovero L, Stipo G, De Stefano M. Intrados strengthening of brick masonry arches with different FRCM composites: Experimental and analytical investigations. Compos. Struct. 2017; 176:898–909. https://doi.org/10.1016/j.compstruct.2017.06.023.

[8] Alecci V, Misseri G, Rovero L, Stipo G, De Stefano M, Feo L, Luciano R. Experimental investigation on masonry arches strengthened with PBO-FRCM composite. Compos. Part B 2016; 100:228–239. https://doi.org/10.1016/j.compositesb.2016.05.063.

[9] Greco F, Leonetti L, Luciano R, Trovalusci P. Multiscale failure analysis of periodic masonry structures with traditional and fiber-reinforced mortar joints. Compos. Part B 2017; 118:75–95. https://doi.org/10.1016/j.compositesb.2017.03.004.

[10] Misseri G, Rovero L, Stipo G, Barducci S, Alecci V, De Stefano M. Experimental and analytical investigations on sustainable and innovative strengthening systems for masonry arches. Compos. Struct. 2019; 210:526–537. https://doi.org/10.1016/j.compstruct.2018.11.054.

[11] Cevallos O.A, Olivito R.S, Codispoti R, Ombres L. Flax and polyparaphenylene benzobisoxazole cementitious composites for the strengthening of masonry elements subjected to eccentric loading. Compos. Part B 2015; 71:82–95. https://doi.org/10.1016/j.compositesb.2014.10.055.

[12] Oliveira D.V, Basilio I, Lourenço P.B. Experimental Behavior of FRP Strengthened Masonry Arches. J. Compos. Constr. 2010; 14(3):312–322 https://doi.org/10.1061/(ASCE)CC.1943-5614.0000086.

[13] Triantafillou, T.C., Papanicolaou, C.G. Shear strengthening of reinforced concrete members with textile reinforced mortar (TRM) jackets. Mater. Struct. 2006; 39:93–103 https://doi.org/10.1007/s11527-005-9034-3.

[14] Garmendia L, San-José J.T, García D, Larrinaga P. Rehabilitation of masonry arches with compatible advanced composite material. Constr. Build. Mater. 2011; 25(12):4374–4385. https://doi.org/10.1016/j.conbuildmat.2011.03.065.

[15] Zampieri P, Simoncello N, Tetougueni C.D, Pellegrino C. A review of methods for strengthening of masonry arches with composite materials. Eng. Struct. 2018; 171:154–169. https://doi.org/10.1016/j.engstruct.2018.05.070.

[16] Tsonos A.D.G. A new method for earthquake strengthening of old R/C structures without the use of conventional reinforcement. Struct. Eng. Mech. 2014; 52(2):391–403. https://doi.org/10.12989/sem.2014.52.2.391.

[17] Altun F, Haktanir T, Ari K. Effects of steel fiber addition on mechanical properties of concrete and RC beams. Constr. Build. Mater. 2007; 21(3):654–661. https://doi.org/10.1016/j.conbuildmat.2005.12.006.

[18] Hassan AMT, Jones SW, Mahmud GH. Experimental test methods to determine the uniaxial tensile and compressive behaviour of ultra high performance fibre reinforced concrete (UHPFRC). Constr Build Mater. 2012;37:874–82. https://doi.org/10.1016/j.conbuildmat.2012.04.030.

[19] Ţibea, C., Bompa, D.V. Ultimate shear response of ultra-high-performance steel fibre-reinforced concrete elements. Archiv.Civ.Mech.Eng 20, 49 (2020). https://doi.org/10.1007/s43452-020-00051-z.

[20] Gholampour A, Hassanli R, Mills J.E, Vincent T, Kunieda M. Experimental investigation of the performance of concrete columns strengthened with fiber reinforced

concrete jacket. Constr. Build. Mater. 2019; 194:51–61. https://doi.org/10.1016/j.conbuildmat.2018.10.236.

[21] A Reggia, A Morbi, GA Plizzari. Experimental study of a reinforced concrete bridge pier strengthened with HPFRC jacketing. Engineering Structures 210, 110355 https://doi.org/10.1016/j.engstruct.2020.110355.

[22] L Facconi, F Minelli, S Lucchini, G Plizzari. Experimental study of solid and hollow clay brick masonry walls retrofitted by steel fiber-reinforced mortar coating. Journal of Earthquake Engineering 24 (3), 381-402 https://doi.org/10.1080/13632469.2018.1442264.

[23] L. Facconi, A. Conforti, F. Minelli, G. Plizzari. Improving shear strength of unreinforced masonry walls by nano-reinforced fibrous mortar coating. Materials and Structures (2015) 48:2557–2574. DOI 10.1617/s11527-014-0337-0

[24] Simoncello N, Zampieri P, Gonzalez-libreros J, Pellegrino C. Experimental behaviour of damaged masonry arches strengthened with steel fiber reinforced mortar (SFRM). Comp. Part B 2019; 177:107386. https://doi.org/10.1016/j.compositesb.2019.107386.

[25] Sevil T, Baran M, Bilir T, Canbay E. Use of steel fiber reinforced mortar for seismic strengthening. Constr. Build. Mater. 2011; 25(2):892–899. https://doi.org/10.1016/j.conbuildmat.2010.06.096.

[26] Y. Zhang, P. Zhu, Z. Liao, L. Wang. Interfacial bond properties between normal strength concrete substrate and ultra-high performance concrete as a repair material. Constr. Build. Mater. 2020; 235:117431. https://doi.org/10.1016/j.conbuildmat.2019.117431.

[27] Saddam H. Abo Sabah, Nur L. Zainal, Norazura Muhamad Bunnori, Megat A. Megat Johari, Mohd H. Hassan. Interfacial behavior between normal substrate and green ultra-high-performance fiber-reinforced concrete under elevated temperatures. Structural Concrete. (2019) 20:1896–1908 DOI: 10.1002/suco.201900152.

[28] Y. Zhanga, C. Zhanga, Y. Zhu, J. Cao, X. Shao. An experimental study: various influence factors affecting interfacial shear performance of UHPC-NSC. Constr. Build. Mater. 2020; 236:117480. https://doi.org/10.1016/j.conbuildmat.2019.117480.

[29] UNI EN 998-2_2016. Specification for Mortar for Masonry - Part 2_ Masonry Mortar.

[30] UNI-EN 1015-11. Methods of Test for Mortar for Masonry - Determination of Flexural and Compressive Strength of Hardened Mortar.

[31] UNI EN 13412:2007. Products and Systems for the Protection and Repair of Concrete Structures - Test Methods - Determination of Modulus of Elasticity in Compression.

[32] BS EN 771-1:2011. Specification for masonry units - Part 1 : Clay masonry units.

[33] BS EN 1052-1:1999. Methods of test for masonry - Part 1 : Determination of compressive strength.

[34] EN 1996-1 1 2005;1. Eurocode6. Structures G Rules for Reinforced and Unreinforced Masonry.

[35] Thamboo J, Dhanasekar M. Correlation between the performance of solid masonry prisms and wallettes under compression. J. Build. Eng. 2019; 22:429–438. https://doi.org/10.1016/j.jobe.2019.01.007.

[36] BS EN 14651:2005. Test method for metallic fibre concrete — Measuring the flexural tensile strength (limit of proportionality (LOP), residual).

[37] CNR-DT 204/2006. Istruzioni per la Progettazione, l'Esecuzione ed il Controllo di Strutture di Calcestruzzo Fibrorinforzato.

[38] Xu B.W, Shi H.S. Correlations among mechanical properties of steel fiber reinforced concrete. Constr. Build. Mater. 2009; 23(12):3468–3474. https://doi.org/10.1016/j.conbuildmat.2009.08.017.

[39] Yoo D.Y, Banthia N, Yoon Y.S. Predicting the flexural behavior of ultra-high-performance fiber-reinforced concrete. Cem. Concr. Compos. 2016; 74:71–87. https://doi.org/10.1016/j.cemconcomp.2016.09.005.

[40] Mukhtar F.M, Faysal R.M. A review of test methods for studying the FRP-concrete interfacial bond behavior. Constr. Build. Mater. 2018; 169:877–887. https://doi.org/10.1016/j.conbuildmat.2018.02.163.

[41] Hadigheh S.A, Gravina R.J, Setunge S. Identification of the interfacial fracture mechanism in the FRP laminated substrates using a modified single lap shear test. Eng. Fract. Mech. 2015; 134:317–329. https://doi.org/10.1016/j.engfracmech.2014.12.001.

[42] Falope F.O, Lanzoni L, Tarantino A.M. Double lap shear test on steel fabric reinforced cementitious matrix (SFRCM). Compos. Struct. 2018; 201:503–513. https://doi.org/10.1016/j.compstruct.2018.06.001.

[43] D'Antino T, Sneed L.H, Carloni C, Pellegrino C. Effect of the inherent eccentricity in single-lap direct-shear tests of PBO FRCM-concrete joints. Compos. Struct. 2016; 142:117–129. https://doi.org/10.1016/j.compstruct.2016.01.076.

[44] Sneed L.H, D'Antino T, Carloni C, Pellegrino C. A comparison of the bond behavior of PBO-FRCM composites determined by double-lap and single-lap shear tests. Cem. Concr. Compos. 2015; 64:37–48. https://doi.org/10.1016/j.cemconcomp.2015.07.007.

[45] Bertolesi E, Milani G, Fagone M, Rotunno T, Grande E. Micro-mechanical FE numerical model for masonry curved pillars reinforced with FRP strips subjected to single lap shear tests. Compos. Struct. 2018; 201:916–931. https://doi.org/10.1016/j.compstruct.2018.06.111.

[46] Rotunno T, Fagone M, Bertolesi E, Grande E, Milani G. Single lap shear tests of masonry curved pillars externally strengthened by CFRP strips. Compos. Struct. 2018; 200:434–448. https://doi.org/10.1016/j.compstruct.2018.05.097.

[47] de Carvalho Bello C.D, Boem I, Cecchi A, Gattesco N, Oliveira D.V. Experimental tests for the characterization of sisal fiber reinforced cementitious matrix for strengthening masonry structures. Constr. Build. Mater. 2019; 219:44–55. https://doi.org/10.1016/j.conbuildmat.2019.05.168.

[48] Ombres L, Iorfida A, Mazzuca S, Verre S. Bond analysis of thermally conditioned FRCM-masonry joints. Measurement 2018; 125:509–515. https://doi.org/10.1016/j.measurement.2018.05.021.

[49] Franzoni E, Gentilini C, Santandrea M, Carloni C. Effects of rising damp and salt crystallization cycles in FRCM-masonry interfacial debonding : Towards an accelerated laboratory test method. Constr. Build. Mater. 2018; 175:225–238. https://doi.org/10.1016/j.conbuildmat.2018.04.164.

[50] G.B. Barbat, M. Cervera, M. Chiumenti, E. Espinoza, Structural size effect: Experimental, theoretical and accurate computational assessment, Engineering Structures, Volume 213, 2020, https://doi.org/10.1016/j.engstruct.2020.110555.

[51] Popovics, S. A numerical approach to the complete stress-strain curve of concrete. Cement and Concrete Research (1973); 3(5):583–599. https://doi.org/10.1016/0008-8846(73)90096-3.

[52] CNR-DT 200 R1/2013. Istruzioni per la Progettazione, l'Esecuzione ed il Controllo di Interventi di Consolidamento Statico mediante l'utilizzo di Compositi Fibrorinforzati.

[53] B. Ghiassi, G. Marcari, D.V. Oliveira, P. B. Lourenço. Numerical analysis of bond behavior between masonry bricks and composite materials. Eng. Struct. (2012). 43:210-220. https://doi.org/10.1016/j.engstruct.2012.05.022.

[54] Vecchio, F. J., and Collins, M. P. (1986). Modified compression-field theory for reinforced concrete elements subjected to shear. J. Am. Concrete Inst. 83, 219–231.